RSC Advances

PAPER

View Article Online
View Journal | View Issue

Cite this: *RSC Adv.*, 2026, **16**, 20883

Visible-light photocatalytic water splitting performance of V and Co codoped $SrTiO_3$: a first-principles study

Chuang Li, Jiazheng Qiu, Jianfeng Wen and Xianwen Luo*

This study employs first-principles calculations to investigate the effects of V and Co co-doping on the electronic structure, optical properties, and photocatalytic activity of $SrTiO_3$. The calculation results indicate that a positive defect binding energy and shortened V–O/Co–O bond lengths enhance the structural stability of the co-doped system. An intermediate band is introduced into the forbidden gap of the material *via* the strong hybridization between V-3d, Co-3d and O-2p orbitals, and the band gap is significantly narrowed from 3.2 eV of the pristine phase to 2.5 eV, 2.17 eV, and 1.95 eV for the near, medium, and far configurations, respectively, upon the scissors operator correction. This modification leads to a significant red-shift in the optical absorption spectrum, with the absorption edge extending from 390 nm to 650 nm and the emergence of new absorption peaks, thereby improving the light-harvesting capability in the visible region. Furthermore, band edge position analysis shows that its band edges are well-matched with the redox potentials of water, possessing the necessary conditions for water splitting. This work provides important theoretical guidance for the design of novel and efficient visible-light photocatalytic materials.

Received 6th February 2026
Accepted 28th March 2026

DOI: 10.1039/d6ra01052k

rsc.li/rsc-advances

1. Introduction

Perovskites constitute a class of compounds with the general chemical formula ABX_3, wherein A and B represent metal cations, and X denotes oxygen or a halogen. In ABO_3-type perovskites specifically, the conduction band is predominantly composed of the 3d orbitals of the B-site cation, while the valence band arises from the 2p orbitals of oxygen.[1] The distinctive crystal structure of perovskites underpins their extensive utility in catalysis, as well as in solid-state devices including solar cells and solid oxide fuel cells.[2] Notwithstanding the high catalytic efficiency exhibited by organic perovskites, their practical deployment is hindered by inherent instability and toxicity concerns.[3] In contrast, the inorganic perovskite strontium titanate ($SrTiO_3$) demonstrates exceptional stability and significant catalytic potential. It exhibits remarkable efficacy in decomposing hazardous chemicals within industrial exhaust gases,[4,5] degrading organic pollutants in aqueous environments,[6,7] and facilitating catalytic hydrogen production,[8,9] thus holding substantial promise for environmental remediation applications.

However, $SrTiO_3$ exhibits limited light absorption confined to ultraviolet wavelengths below 385 nm due to its wide bandgap of 3.2 eV, which consequently leads to low solar energy utilization efficiency. This limitation poses a critical obstacle to the large-scale application of $SrTiO_3$ in photocatalysis.[10–12] Therefore, doping modification is commonly employed to engineer its bandgap and broaden the light absorption range.[13,14]

Doping modification represents a cornerstone strategy for tailoring material properties. Conventional chemical doping methods, such as hydrothermal synthesis[15] and sol–gel processing,[16] are widely employed but suffer from inherent limitations including prolonged preparation cycles and poor controllability over reaction processes.[17,18] In contrast, doping based on ion implantation, the so-called physical doping,[19–21] leverages its non-chemical nature to enable precise control over dopant concentration and spatial distribution,[22] significantly enhancing dopant purity and structural stability,[23] as illustrated in Fig. 1. Existing studies report that Rh–Sb co-doped $SrTiO_3$ photocatalysts synthesized *via* solid-state reaction can achieve efficient acetaldehyde degradation.[24] However, optimizing critical process parameters, including grinding duration and Rh/Sb doping ratios, relies on extensive repetitive experimentation, substantially increasing research complexity. Furthermore, chemical doping necessitates multiple sample replications for different dosages, introducing additional uncertainties in fabrication. Ion implantation doping, conversely, facilitates simultaneous substitution at multiple Ti sites within the perovskite lattice while ensuring stringent dosage control. For instance, Mo–P co-doping at Ti sites in $SrTiO_3$ extends the optical absorption edge beyond 600 nm.[25] In addition, recent

Key Laboratory of Low-dimensional Structural Physics and Application, College of Physics and Electronic Information Engineering, Guilin University of Technology, Guilin 541004, China. E-mail: luoxw@glut.edu.cn

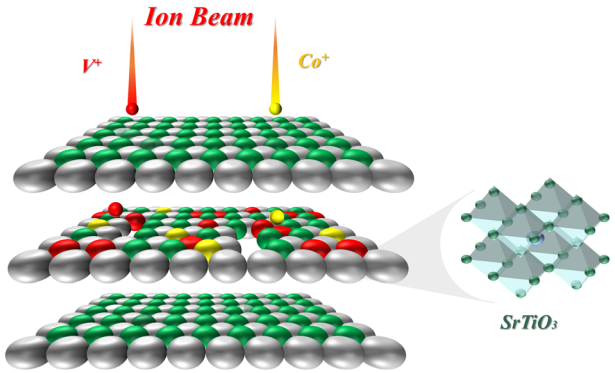

Fig. 1 Schematic diagram of ion implantation on $SrTiO_3$. (drawn by the OneKey 10 plugin in Microsoft PowerPoint).

first-principles studies have predicted other novel systems, such as square-octagon haeckelites[26] and SiS–Al_2SO/blueP-Al_2SO van der Waals heterojunctions,[27] showing great promise for solar-to-hydrogen conversion, which provides valuable theoretical guidance for the design of high-efficiency photocatalysts. Comparative studies on Fe-ion beam irradiation of RP-phase $SrTiO_3$ have elucidated the differential contributions of Fe occupancy at Sr *versus* Ti sites to bandgap reduction.[28] Nevertheless, these ion implantation experiments predominantly focus on single-atom doping effects, neglecting the influence of dual-atom doping and distinct site-occupancy configurations at Ti sites on bandgap modulation.[29] Therefore, this study examines the effects of various V and Co co-doping configurations at Ti sites on the band gap of $SrTiO_3$. The selection of these two elements is supported by solid scientific evidence and unique merits for material modification. V and Co have a high degree of ionic radius matching with the host Ti^{4+}, and their substitutional doping only induces slight lattice distortion, which preserves the crystal structure stability of $SrTiO_3$. The synergistic regulation effect of V–Co co-doping still lacks systematic theoretical investigation, which is exactly the core research motivation of this work.

This study employs first-principles calculations to investigate the effects of V and Co co-doping on the electronic structure and photocatalytic activity of $SrTiO_3$, where V and Co atoms substitute for Ti sites in the lattice. The research focuses on the electronic and optical properties of the system. The electronic structure of the co-doped system was analyzed and compared to gain a deeper understanding of the intermediate states that reduce the band gap. The synergistic effect on redox capability was also explored. To verify its feasibility for photocatalytic water splitting, the alignment of the band edge positions with the redox potentials of water was carefully analyzed. The results indicate that V and Co co-doping is an effective strategy for enhancing the photocatalytic performance of $SrTiO_3$ and shows promising application prospects in the field of visible-light photocatalysis.

2. Computational methods

2.1 DFT calculation

This study focuses on the cubic phase of $SrTiO_3$ with space group *Pm*-3*m* at room temperature, which exhibits a stable octahedral framework with a lattice constant of 3.905 Å.[30] In this structure, vertex-sharing oxygen octahedra form the unit cell, with Sr occupying the octahedral interstitial sites (0, 0, 0), Ti positioned at the octahedral center (1/2, 1/2, 1/2), and O located at (0, 1/2, 1/2). To precisely simulate the synergistic modulation of electronic structures by V and Co co-doping, a 2 × 2 × 2 supercell model containing 40 atoms (8 Sr, 8 Ti, and 24 O atoms) was constructed,[31] as illustrated in Fig. 2. Geometric optimization was carried out on pristine cubic $SrTiO_3$, yielding an optimized lattice constant of 3.942 Å with a minor deviation of 1% relative to the experimental value. This finding confirms the validity of the employed computational approach.

This study systematically investigates the synergistic modulation mechanism of V and Co co-doping on the electronic structure and optical properties of $SrTiO_3$ using first-principles calculations based on density functional theory.[32,33] The calculations were performed using the VASP software package, employing the projector augmented wave (PAW) method to describe ion–electron interactions and the Perdew–Burke–Ernzerhof (PBE) functional to treat exchange-correlation energy.[34] Electronic structure calculations utilized a plane-wave cutoff energy of 520 eV and a 6 × 6 × 6 Monkhorst–Pack *k*-point mesh.[35] Geometric optimization was conducted using the conjugate gradient algorithm. A 2 × 2 × 2 supercell of $SrTiO_3$ was modeled, where two Ti atoms were substituted with V and Co respectively to achieve co-doped $SrTiO_3$. All lattice parameters and atomic positions were fully relaxed until residual forces fell below 0.02 eV $Å^{-1}$, with the optimized electronic energy convergence criterion set to 10^{-6} eV.[36] In addition, it is well

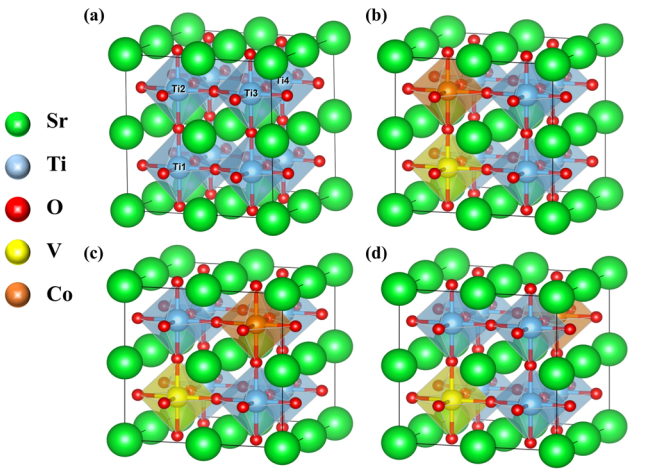

Fig. 2 The 2 × 2 × 2 supercell structure of (a) the pristine cubic perovskite $SrTiO_3$, and the (V + Co) co-doped $SrTiO_3$ in the (b) near, (c) medium, (d) and far configurations. The green, light blue, and red spheres represent Sr, Ti, and O atoms, respectively. The V and Co dopant atoms are marked in yellow and brown, respectively. (The crystal structures were visualized using VESTA software).

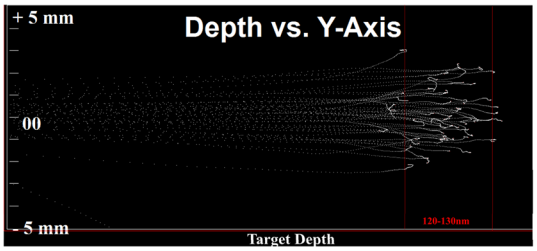

Fig. 3 Trajectory diagram of ion beam injection into $SrTiO_3$ simulated by TRIM program.

established that the generalized gradient approximation (GGA) tends to underestimate the band gap of semiconductors when describing the strong correlation effects of d-electrons. Therefore, the GGA + U approach was employed in this work.[37] The on-site Coulomb interaction parameter U for Ti 3d states was set to 4.3 eV, while a value of 3 eV was adopted for the 3d states of both V and Co.[38] All calculations involving the magnetic dopants V and Co were performed in a spin-polarized manner.

2.2 Feasibility analysis of ion implantation strategy

Due to limited experimental conditions, we employed the TRIM program based on the Monte Carlo method to simulate the stochastic scattering process of ions within the target material.[39] This method, guided by probabilistic statistics theory, approximates solutions to physical problems through extensive random sampling.[40] In the simulation, V and Co ion beams with 10 keV energy were perpendicularly incident on the $SrTiO_3$ target, with ion distribution peaking at approximately 130 nm. The program tracked collision trajectories between ions and target atoms to calculate the energy deposition distribution and spatial position changes of ions within the material. As shown in Fig. 3, the simulation results reveal the depth distribution of incident ions in the target, providing crucial evidence for analyzing implantation-induced defect formation and elemental doping concentration. It is important to note that the TRIM simulation serves solely as a reference for future experimental synthesis design, demonstrating the feasibility of realizing such a structure. The subsequent analysis of the electronic structure and photocatalytic performance is entirely based on first-principles DFT calculations, which serves as the core theoretical basis for predicting material properties.

3. Results and discussion

3.1 Electronic properties

To compare the electronic structures of single-doped and co-doped systems, this study first investigates the electronic properties of V or Co single-doped $SrTiO_3$ by calculating their band structures and density of states (DOS), as presented in Fig. 4. Fig. 4(a) and (b) respectively illustrate the DOS characteristics of V and Co single doped systems, revealing that both introduce mid gap states near the conduction band minimum (CBM) and valence band maximum (VBM), consistent with literature reports.[41] Specifically, in Fig. 4(a), the impurity states of the V-doped system originate from the hybridization between V-3d and O-2p orbitals, with the dominant orbital at the CBM shifting from Ti-3d to V-3d after doping. In contrast, Fig. 4(b) shows that the energy states near the VBM of the Co-doped system are primarily dominated by Co-3d orbitals, accompanied by minor O-2p contributions. Notably, the spin channels of both doped systems exhibit significant differences: the spin-up channel demonstrates a narrower band gap (E_g) due to easier electron occupation of low energy levels near the CBM/VBM, whereas the spin-down channel displays an enlarged band gap as electrons occupy higher energy levels. Furthermore, the spin polarization phenomenon observed in the DOS plots of Fig. 4(a) and (b) indicates ferromagnetism in the systems, which stems from the d electron spin polarization characteristics of the V/Co dopant atoms. Similarly, the ferromagnetism induced by transition metal doping has been widely documented in other semiconductor systems, such as V or Cr doped MoI_3 (ref. 42) and Cr or Fe doped Mo_8S_{12}.[43]

Based on the electronic structure analysis of single-doped systems, we calculated the band structures of V and Co co-doped $SrTiO_3$ with various configurations. These were compared with the band structure of pristine $SrTiO_3$ to further investigate the influence of impurity bands, as shown in Fig. 5. Fig. 5(a) reveals that the calculated E_g of pure $SrTiO_3$ is 2.18 eV, consistent with previous theoretical reports[44] but significantly lower than the experimental value of 3.2 eV. This discrepancy arises from the inherent limitations of the GGA method.[45] Nevertheless, GGA remains reliable for describing fundamental features of band structures and predicting bandgap variation trends,[46] thus enabling its application in subsequent comparative analyses of co-doped systems.

As shown in Fig. 5(a) for pristine $SrTiO_3$, the band characteristics of the V and Co co-doped systems with various configurations were subsequently analyzed. Fig. 5(b)–(d) demonstrate that, compared to pure $SrTiO_3$, all (V + Co) co-doped systems form intermediate bands (IBs) within the bandgap. IBs can act as a springboard to help excite valence electrons to the CBM under the illumination of a long-wave light source, thereby increasing the optical absorption. This beneficial effect dominates because the delocalized nature of the IBs inhibits their role as recombination centers.

Specifically, V and Co co-doping introduce intermediate states near the CBM and VBM, respectively. This aligns with the impurity level positions observed in V or Co single-doped $SrTiO_3$ in Fig. 4. The formation mechanism originates from the charge compensation effect: when V, acting as a donor impurity, substitutes Ti, it provides excess electrons that occupy the conduction band as charge carriers; conversely, Co, as an acceptor impurity lacking valence electrons, captures electrons from the valence band, generating holes therein.

Compared to single doping, (V + Co) co-doping exhibits a distinct synergistic effect by integrating the characteristics of individual dopants. It simultaneously introduces impurity levels near both the CBM and VBM, a feature unattainable by single doping. This enables precise modulation of $SrTiO_3$'s electronic structure and effectively narrows the bandgap. Further analysis of Fig. 5(b)–(d) reveals that in (V + Co) co-doped

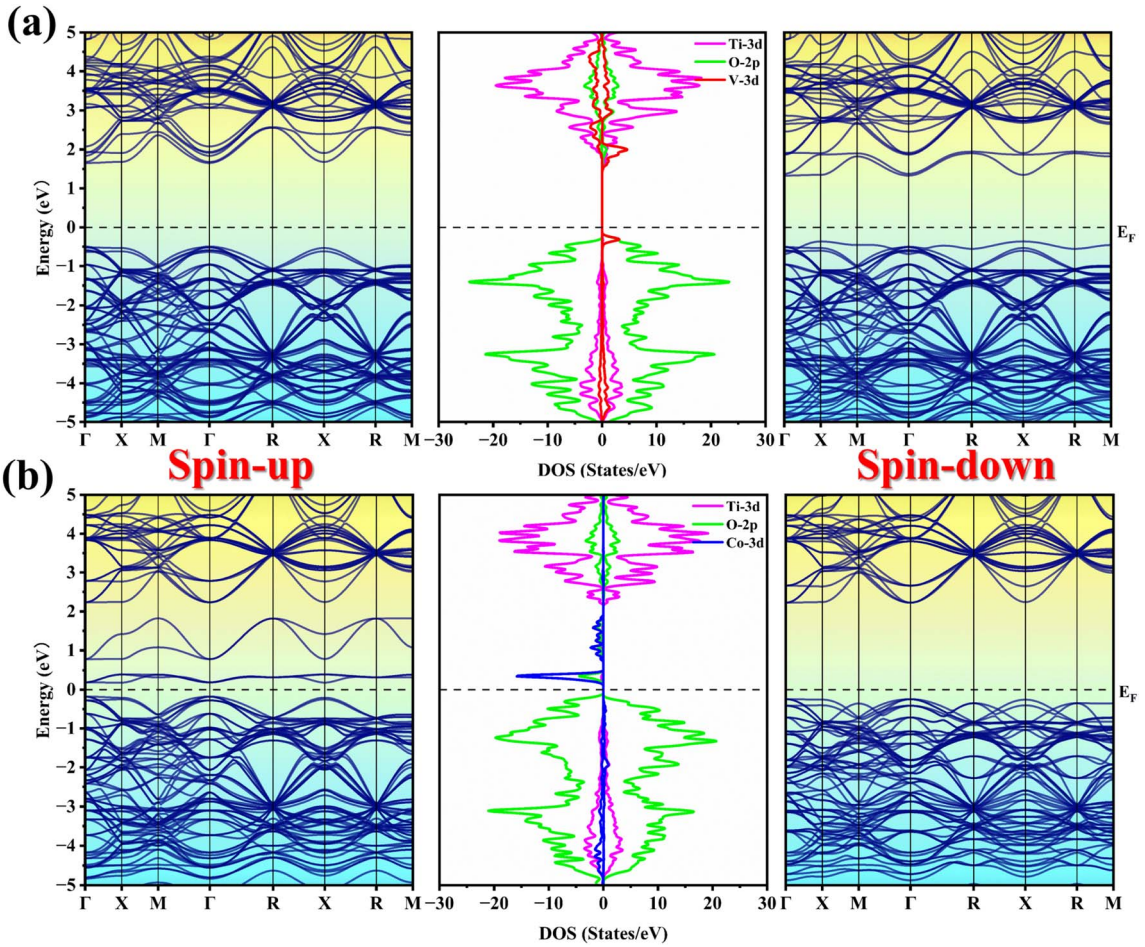

Fig. 4 Calculated spin-polarized band structures (with spin-up and spin-down channels shown on the left and right, respectively) and total DOS for (a) V-doped and (b) Co-doped $SrTiO_3$.

systems, the dopant-induced states below the Fermi level are fully occupied. The fully occupied intermediate band states adjacent to the VBM provide a two-step pathway for optical excitation to the CBM, which significantly enhances light absorption and mitigates carrier recombination compared to localized states in single-doped systems. Moreover, due to the synergistic effect of charge compensation, these fully occupied intermediate bands are stabilized energetically and positioned close to the VBM. For the intermediate and distant configurations in Fig. 5(c) and (d), the CBM exhibits a slight downward shift compared to the neighboring configuration, further narrowing the fundamental bandgap of the material.

Fig. 6 illustrates the calculated TDOS and PDOS. For pristine $SrTiO_3$, as depicted in Fig. 6(a), the VBM is formed mainly by O-2p orbitals, whereas the CBM consists predominantly of Ti-3d states. This electronic structure aligns with established findings in the literature.[47] Given the minimal contribution of Sr atomic orbitals to the upper valence band and lower conduction band, their energy states are omitted from the doped density of states plots. In contrast, Fig. 6(b)–(d) demonstrate that across all three investigated (V + Co) co-doped $SrTiO_3$ configurations, both VBM and CBM exhibit systematic shifts toward the Fermi level. Corresponding to the band structures in Fig. 5(b)–(d), this redistribution of energy levels results in significant bandgap narrowing, with measured values of 1.48 eV, 1.15 eV, and 0.93 eV for the three configurations, respectively. The observed bandgap reduction facilitates electron transitions from the VBM to the CBM by lowering the excitation energy, thereby broadening the material's optical absorption spectrum.

Further analysis of Fig. 6(b)–(d) reveals IBs near the valence band in all three (V + Co) co-doped configurations. The formation of these impurity bands primarily stems from orbital hybridization between Co-3d and O-2p orbitals, as the energy of Co-3d orbitals lies below that of Ti-3d orbitals. Notably, additional energy levels originating from V-3d and O-2p state hybridization are observed near the CBM, indicating strong V–O interactions within the (V + Co) co-doped $SrTiO_3$ structure. This interaction serves as the key factor driving the CBM shift toward the Fermi level. Moreover, the positions of impurity levels introduced by V and Co co-doping align with those induced by single V or Co doping in Fig. 5. For the (V + Co) co-doped $SrTiO_3$ system, the delocalized and fully occupied intermediate bands generated by p–d orbital coupling effectively reduce the

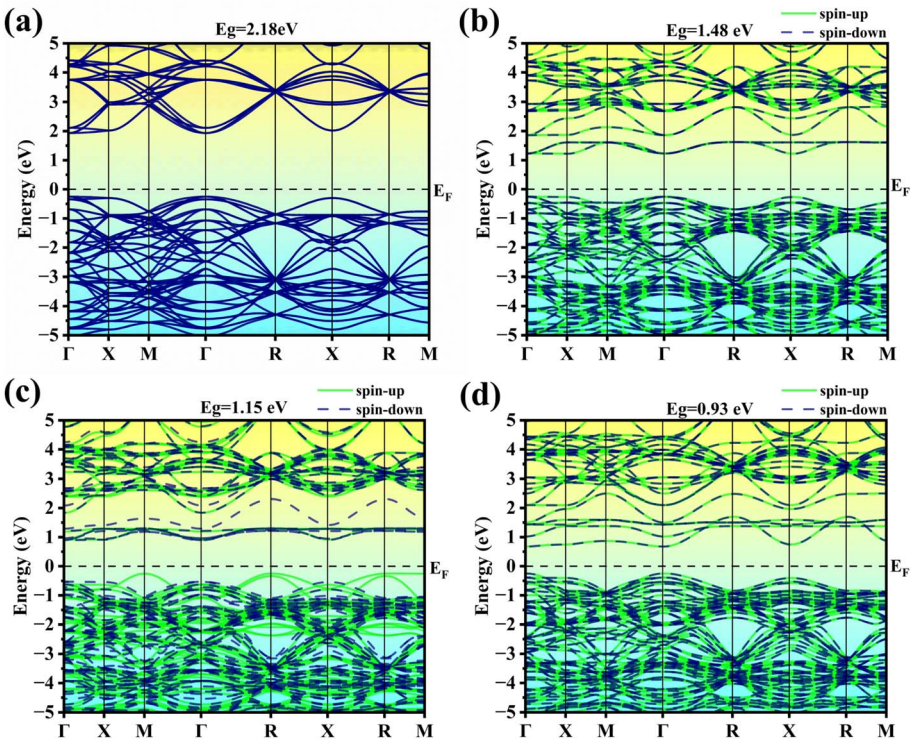

Fig. 5 Calculated band structures for (a) pristine $SrTiO_3$, and for (V + Co) co-doped $SrTiO_3$ in the (b) near, (c) medium, and (d) far dopant configurations.

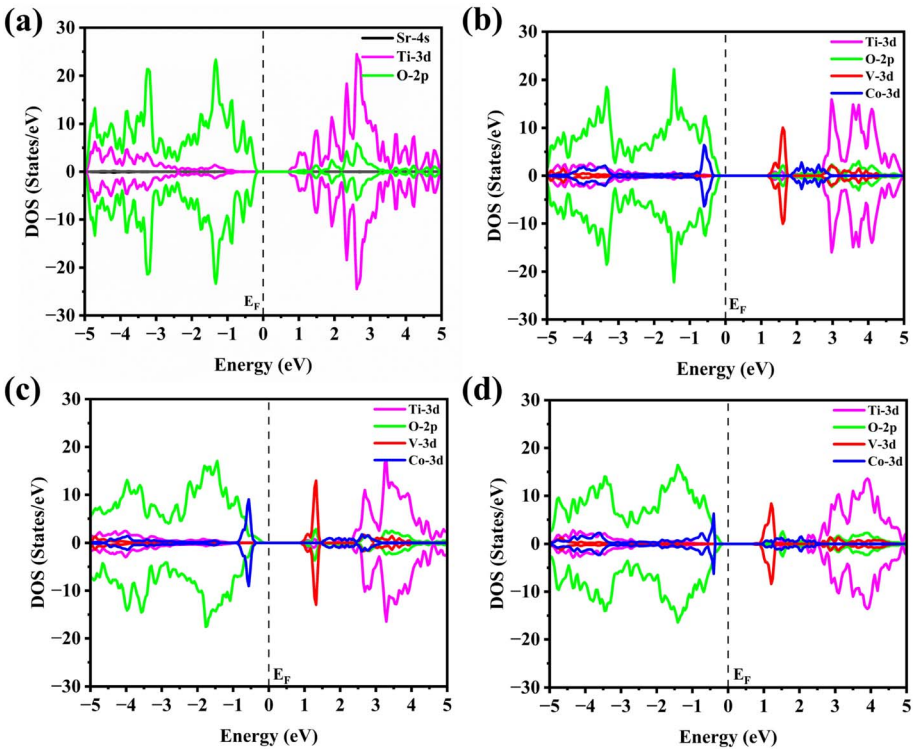

Fig. 6 Total and partial density of states (TDOS and PDOS) for (a) pure $SrTiO_3$, and (V + Co) co-doped $SrTiO_3$ in the (b) near, (c) medium, and (d) far configuration.

material's bandgap width. Collectively, these factors contribute to a potential reduction in the energy required for photoexcitation.

Fig. 7 presents the charge density difference mappings of pristine $SrTiO_3$ and (V + Co) co-doped $SrTiO_3$ systems, in which yellow regions correspond to charge accumulation and cyan regions correspond to charge depletion. For pristine $SrTiO_3$ presented in Fig. 7(a), the charge density is predominantly localized within the bonding regions of Ti–O bonds, exhibiting the characteristic mixed ionic–covalent bonding nature of perovskite oxides, with no distinct extra charge accumulation or depletion observed. Upon substitution of lattice Ti atoms by V and Co dopants, remarkable charge redistribution is triggered in the doped systems: pronounced charge accumulation emerges around the doped V and Co atoms, whereas notable charge depletion is detected at the oxygen atoms adjacent to the dopants. This observation demonstrates that strong orbital hybridization and charge transfer take place between the doped V and Co transition metal atoms and their neighboring oxygen anions, with electrons transferring from the 2p orbitals of oxygen to the 3d orbitals of V and Co. This trend is in excellent agreement with the DOS analysis discussed above, verifying that (V + Co) co-doping enables effective modulation of the bonding properties and electronic structure of $SrTiO_3$. Further comparison of the charge distributions across the three dopant configurations in Fig. 7 reveals that, as the separation between V and Co dopants increases from the near-neighbor configuration in Fig. 7(b) to the far-separated configuration in Fig. 7(d), the localization degree of the charge accumulation regions gradually decreases, and the charge distribution becomes more delocalized. Such a delocalized charge distribution not only mitigates the lattice distortion and internal stress of the system, but also gives rise to the lowest defect formation energy and superior thermodynamic stability for the far-separated dopant configuration.

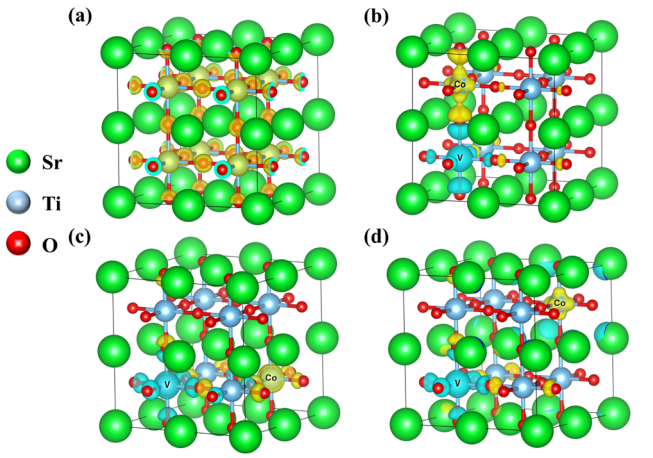

Fig. 7 Calculated charge density difference plots for (a) pristine $SrTiO_3$, and (V + Co) co-doped $SrTiO_3$ in the (b) near, (c) medium, and (d) far dopant configurations. The yellow and cyan regions represent charge accumulation and charge depletion, respectively. The green, gray, and red spheres denote Sr, Ti, and O atoms, respectively.

To assess the experimental difficulty of dopant incorporation into the lattice, we calculated the formation energy (E_f) of different doping systems, where a lower E_f indicates easier doping formation. The formation energy for the (V + Co) co-doped $SrTiO_3$ system is defined as:[48]

$$E_f = E_{doped} - E_{pure} + n_{Ti}\mu_{Ti} - n_V\mu_V - n_{Co}\mu_{Co} \quad (1)$$

where E_{pure} and E_{doped} denote the total energies of the pure $SrTiO_3$ system and (V + Co) co-doped $SrTiO_3$ system, respectively. Here, n_x is the number of dopant atoms of element X, and μ_x is the chemical potential of element X.

In this work, we further considered the influence of the oxygen growth environment (namely O-rich and Ti-rich growth conditions) on the defect formation energy. Under thermodynamic equilibrium between the $SrTiO_3$ phase and the chemical reservoirs of Sr, Ti, and O elements, the following relationship holds:

$$\mu_{Sr} + \mu_{Ti} + 3\mu_O = \mu_{SrTiO_3} \quad (2)$$

where μ_{Sr}, μ_{Ti}, and μ_O are the chemical potentials of Sr, Ti, and O elements, respectively. In this study, μ_{Sr} and μ_{Ti} are calculated from the average energy per atom in the corresponding bulk pure metal crystals. Under O-rich growth conditions, we place an O_2 molecule in a 10 Å × 10 Å × 10 Å cubic periodic box for calculation, and take the average energy per atom of the O_2 molecule to simulate μ_O, while μ_{Ti} is determined by formula (2). Under Ti-rich growth conditions, μ_{Ti} is taken as the average energy per Ti atom in bulk metallic Ti. Table 1 lists the calculated formation energies of the doped $SrTiO_3$ systems. Under Ti-rich conditions, the formation energies of the three (V + Co) co-doped configurations are all negative. This indicates that V and Co atoms preferentially occupy the Ti sites in the $SrTiO_3$ lattice. Such substitution forms a stable co-doped configuration. Thermodynamically, this process is feasible for synthesis. In contrast, under O-rich conditions, the formation energies of the three configurations are all positive. The V and Co co-doping process under O-rich conditions requires overcoming a higher energy barrier. This discrepancy may arise from enhanced interactions between dopant atoms and oxygen atoms under O-rich conditions, or from increased lattice distortion, thus significantly increasing the synthesis difficulty.

Additionally, Fig. 8 presents the evolution of the defect formation energy as a function of the Ti chemical potential for various (V + Co) co-doped $SrTiO_3$ systems. As can be observed from the figure, the defect formation energies of the three

Table 1 Calculated defect formation energies of (V + Co) co-doped $SrTiO_3$ under O-rich and Ti-rich conditions, and the binding energies and dopant separations of defect pairs

Dopants	$E_f^{O\text{-rich}}$ (eV)	$E_f^{Ti\text{-rich}}$ (eV)	E_b (eV)	Distance of dopants (Å)
(V + Co)-near	9.71	−17.202	0.389	3.911
(V + Co)-medium	9.6	−17.312	0.3761	5.531
(V + Co)-far	9.329	−17.583	0.317	6.774

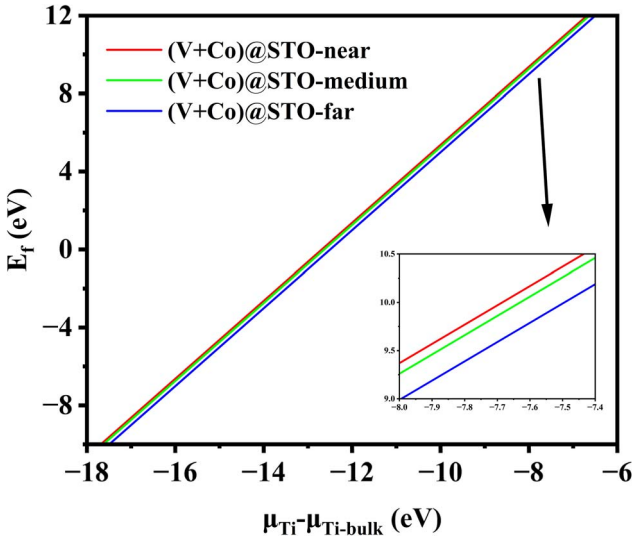

Fig. 8 Variation of defect formation energy for (V + Co) co-doped $SrTiO_3$ with Ti chemical potential.

distinct doped systems increase monotonically with rising Ti chemical potential, which demonstrates that Ti-rich growth conditions are more conducive to the formation of these doping defects. Furthermore, the defect formation energies of the three co-doped systems can be clearly resolved, with the magnitude following the order: $E_f(V + Co)_{near} > E_f(V + Co)_{medium} > E_f(V + Co)_{far}$. Under identical thermodynamic conditions, the farthest-separated co-doped system exhibits the best structural stability, as it possesses the lowest defect formation energy.

To investigate the coupling strength between V–Co doping pairs and their impact on system stability in co-doped models, we calculated the defect pair binding energy (E_b), defined as follows:[49]

$$E_b = E_{V@SrTiO_3} + E_{Co@SrTiO_3} - E_{(V+Co)@SrTiO_3} - E_{SrTiO_3} \quad (3)$$

where $E_{V@SrTiO_3}$, $E_{Co@SrTiO_3}$, $E_{(V+Co)@SrTiO_3}$ and E_{SrTiO_3} represent the total energies of V-doped $SrTiO_3$, Co-doped $SrTiO_3$, (V + Co) co-doped $SrTiO_3$, and pristine $SrTiO_3$, respectively, calculated under identical supercell conditions. A positive E_b value indicates that the co-doping defects are more stable relative to isolated single defects. Table 1 summarizes the distances between V and Co in different configurations and their corresponding E_b values. Distances between adjacent elements on the same surface were directly extracted from CASTEP result files, while distances between other elements were measured as linear distances using visualization software. As shown in Table 1 exhibit positive E_b values, confirming that the co-doped systems possess higher stability than single-doped systems. Further analysis reveals that the E_b values follow the order: $E_b^{(V+Co)\text{-near}} > E_b^{(V+Co)\text{-medium}} > E_b^{(V+Co)\text{-far}}$. This trend can be attributed to the decrease in charge transfer between V and Co as the distance increases. In the near-neighbor configuration, V and Co enable greater charge transfer, forming a stronger charge compensation effect, which releases more energy and significantly enhances system stability. Conversely, in the far-distance configuration, charge transfer is limited, the synergistic effect weakens, and the binding energy decreases accordingly. Therefore, the synergistic effect of V and Co doping is the key factor leading to the enhanced stability of the co-doped system.

In the optimized pure $SrTiO_3$ structure, atomic positions are labeled as shown in Fig. 2(a), with Ti_1–Ti_2, Ti_1–Ti_3, and Ti_1–Ti_4 distances measuring 3.943 Å, 5.576 Å, and 6.829 Å, respectively, and the Ti–O bond length being 1.971 Å. For the three V–Co co-doped systems, the V atom consistently occupies the Ti_1 site, while the Co atom substitutes at the Ti_2, Ti_3, and Ti_4 sites, respectively. As presented in Table 1, the optimized V–Co distances are 3.911 Å, 5.531 Å, and 6.774 Å, all exhibiting significant contraction compared to the corresponding Ti–Ti distances in pure $SrTiO_3$.

Additionally, as shown in Table 2, the Co–O bond lengths in the three co-doped models are 1.9448 Å, 1.9448 Å, and 1.9516 Å, respectively, which are all shorter than the pre-doping Ti–O bond length of 1.971 Å. This reduction arises because Co, as a transition metal, exhibits stronger hybridization between its 3d orbitals and O-2p orbitals, resulting in enhanced covalency and consequently shorter Co–O bond lengths. This indicates that the covalent character of Co–O bonds is stronger than that of Ti–O bonds. Similarly, the V–O bond lengths in all three co-doped cases are markedly shorter than the Ti–O bond length in pure $SrTiO_3$. This is attributed to the smaller atomic radius of V, whose substitution at Ti sites induces local lattice distortion. However, the optimized configurations confirm that the overall perovskite framework remains intact without structural collapse, verifying the structural stability of the doped systems. The relatively short V–O bond lengths suggest strong bonding interactions between V dopant atoms and neighboring O atoms.

Meanwhile, the Ti–O bond lengths in all three co-doped models exceed those in pure $SrTiO_3$. This indirectly reflects weakened bonding capability between Ti and O atoms, likely due to the occupation of Ti sites by V and Co dopants, which alters the electron cloud distribution around Ti and reduces the covalency of Ti–O bonds.

As previously mentioned, the GGA method employed in this study tends to underestimate the bandgap of materials. Although this underestimation does not affect the qualitative analysis of bandgap variations or the investigation of fundamental electronic structure properties, the error introduced by bandgap underestimation becomes significant when predicting

Table 2 Calculated bond lengths of Ti–O, V–O, and Co–O in pure and co-doped $SrTiO_3$ with different configurations

	Bond length (Å)		
Dopants	Ti–O	V–O	Co–O
Pure	1.971	—	—
(V + Co)-near	2.0123	1.9024	1.9448
(V + Co)-medium	2.0217	1.9019	1.9448
(V + Co)-far	2.0133	1.9004	1.9516

semiconductor band edge positions directly related to redox potentials and optical absorption characteristics. To compensate for this systematic deviation, a widely adopted correction strategy is the introduction of a "scissor operator".[50] In this work, the value of the scissor operator (1.02 eV) is set as the difference between the calculated bandgap of pure $SrTiO_3$ (2.18 eV) and its experimental value (3.2 eV).[51] It should be noted that this rigid correction assumes a consistent bandgap underestimation across different systems, which serves as an approximation primarily used to analyze relative bandgap trends rather than providing absolute precise quantitative values. Nevertheless, such qualitative trends are valid for understanding doping effects and guiding experimental design. Table 3 lists the bandgap values before and after applying the scissor operator correction.

The alignment between the band edge positions of a semiconductor and the standard redox potentials of water splitting serves as the core thermodynamic criterion for quantitatively assessing the photocatalytic hydrogen evolution performance of different (V + Co) co-doped $SrTiO_3$ systems. Accordingly, in this work, we calculated the absolute energy levels of the CBM and VBM for all systems using a well-established empirical formula. The calculation formula for the CBM energy level is given by:[52]

$$E_{CB} = X - \frac{1}{2}E_g - E_0 \quad (4)$$

In this equation, E_g is the band gap value of the target semiconductor system obtained from our first-principles calculations. X represents the absolute electronegativity of the perovskite oxide, which is calculated as the geometric mean of the absolute electronegativity of each constituent atom in the system. E_0 refers to the energy of free electrons on the hydrogen scale (~4.5 eV).

The VBM energy level of each system was further derived from the intrinsic linear relationship between the CBM energy level and the band gap, as shown in the following equation:

$$E_{VB} = E_{CB} + E_g \quad (5)$$

Based on the above-calculated absolute CBM and VBM energy levels, we plotted the band alignment diagrams of three distinct (V + Co) co-doped $SrTiO_3$ systems and pristine $SrTiO_3$, with all energy levels calibrated against the standard redox potentials of water splitting. The corresponding band alignment results are summarized and presented in Fig. 9. The calculated results indicate that for pure $SrTiO_3$, the CBM is higher than the water reduction potential, and the VBM is lower than the water oxidation potential, which is consistent with previous studies.[53] In all three (V + Co) co-doped $SrTiO_3$ systems, impurity bands appear within the forbidden gap. These fully occupied bands can act as "stepping stones" connecting the VBM and CBM, enabling photogenerated electrons to be directly excited from the impurity band to the conduction band. As shown in Fig. 9, (V + Co) co-doping effectively narrows the band gap by introducing delocalized energy levels, while also significantly perturbing the positions of the VBM and CBM. In the tri-(V + Co) co-doped $SrTiO_3$ system, the VBM and CBM positions straddle the water redox potentials, simultaneously satisfying the thermodynamic requirements for photocatalytic water splitting and reducing the band gap. These results demonstrate that (V + Co) co-doping can enhance the photocatalytic activity of $SrTiO_3$.

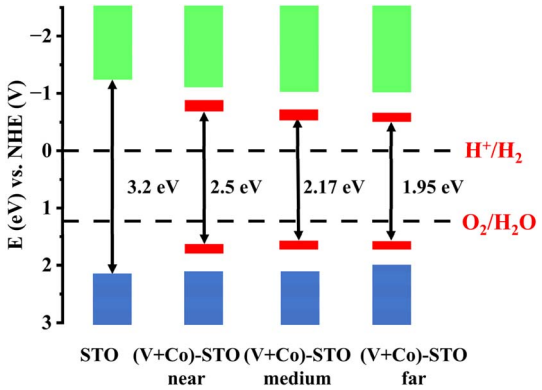

Fig. 9 Band alignment diagram of pure and V–Co co-doped $SrTiO_3$ with respect to water redox potentials. (Blue: valence band, red: intermediate band states, green: conduction band).

Table 3 The E_g of pure and doped $SrTiO_3$, with and without scissors operator correction

Dopants	E_g (eV)	E_g (eV) with scissor operator (1.02 eV)
Pure	2.18	3.2
(V + Co)-near	1.48	2.5
(V + Co)-medium	1.15	2.17
(V + Co)-far	0.93	1.95

3.2 Optical properties

The optical absorption coefficient was derived from the imaginary part of the dielectric function under the independent particle approximation (IPA), as described by the following formula:[54]

$$\alpha(\omega) = \sqrt{2}\omega\sqrt{\sqrt{\varepsilon_1(\omega)^2 + \varepsilon_2(\omega)^2} - \varepsilon_1(\omega)} \quad (6)$$

where ω is the angular frequency, and $\varepsilon_1(\omega)$and $\varepsilon_2(\omega)$ are the real and imaginary parts of the complex dielectric function, respectively. Due to the tensor nature of the dielectric function, the average values of ε_x, ε_y, and ε_z were calculated.

It is important to note that the IPA neglects excitonic effects and local field effects. For materials like $SrTiO_3$ with high dielectric constants, the IPA can reasonably describe the trend of optical absorption, though it may underestimate the absorption intensity. Excitonic effects, which are not considered here, could affect the precise prediction of exciton binding energies, but they do not alter the qualitative conclusions regarding bandgap narrowing and the redshift of the absorption edge.

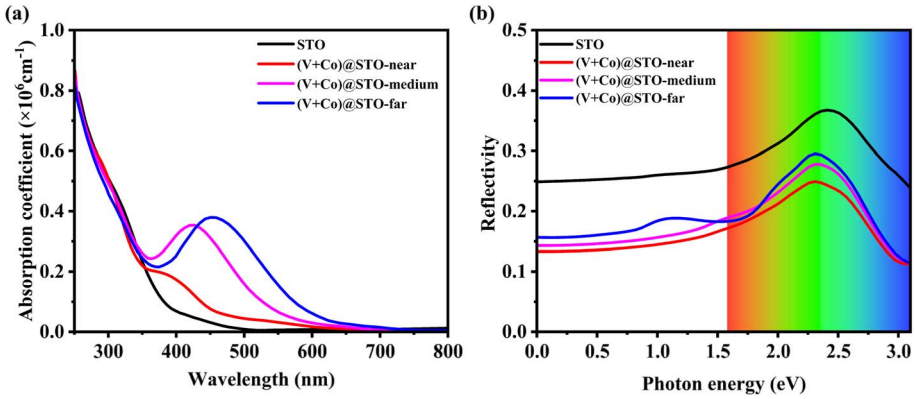

Fig. 10 (a) Optical absorption spectra and (b) reflection spectra of pure and (V + Co) co-doped $SrTiO_3$.

We calculated the optical absorption coefficients of three (V + Co) co-doped $SrTiO_3$ systems and compared them with the results of pure $SrTiO_3$, as shown in Fig. 10(a). The calculation results show that the optical absorption coefficient of pure $SrTiO_3$ is consistent with previous experimental and theoretical results,[55] and its absorption is limited to the ultraviolet region, with almost no activity in the visible light region.

In contrast, all (V + Co) co-doped $SrTiO_3$ systems exhibit significant optical absorption activity in the visible light region, with their absorption spectra showing obvious redshift. New absorption peaks appear at 300 nm, 420 nm, and 455 nm for the near, medium, and far configured systems, respectively. Moreover, as the configuration changes from near to far, the intensity of the absorption peaks progressively increases, which strongly correlates with the gradual narrowing of the band gap. This phenomenon is mainly attributed to the introduction of fully occupied IBs near the VB and CB, which promote electron transitions to the conduction band.

Notably, the position of the new absorption peaks correlates with the location of the IBs within the bandgap, such that the closer the IB is to the VB or CB, the more the absorption spectrum shifts toward longer wavelengths. Furthermore, the absorption intensity in the visible light region for the medium and far configurations is significantly higher than that for the near configuration, which is due to their smaller bandgap widths, extending the maximum absorption edge from 390 nm to 650 nm. In summary, co-doping $SrTiO_3$ with V and Co significantly enhances its optical absorption, highlighting its promise as a visible light photocatalyst.

Furthermore, reflectance and its reflective property are also important characteristics for evaluating the application performance of photocatalytic materials. Fig. 10(b) shows the reflectance of pure $SrTiO_3$ and three (V + Co) co-doped $SrTiO_3$ systems in the visible light region. The results indicate that pure $SrTiO_3$ exhibits a reflectance of approximately 35% across the entire visible light range. In contrast, the reflectance of the near, medium, and far co-doped configurations in the visible light region drops significantly to about 25%. This decrease in reflectance can be attributed to the enhanced performance of the (V + Co) co-doped $SrTiO_3$ system. Overall, the co-doped $SrTiO_3$ material not only demonstrates high light absorption capacity in the visible light range but also possesses low reflectance. The synergy between these two factors significantly improves the material's solar light collection efficiency, providing strong support for its application in practical photovoltaic devices.

4. Conclusion

This study employs first-principles calculations to systematically investigate the effects of V and Co co-doping on the electronic structure and photocatalytic performance of $SrTiO_3$. The calculation results indicate that the E_b for all co-doped configurations is positive and decreases with increasing V–Co distance, which confirms that the co-doped system possesses higher structural stability than single-doped systems. The co-doping of V and Co induces strong hybridization among V-3d, Co-3d, and O-2p orbitals, forming a fully occupied and highly delocalized IBs near the valence and conduction band edges. This band facilitates the separation of photogenerated electron–hole pairs and reduces the probability of electrons being trapped by defects near the conduction band. Furthermore, the combined effect of V–O hybridization and Co–O coupling effectively narrows the band gap of $SrTiO_3$ from 3.2 eV to 2.5 eV, 2.17 eV, and 1.95 eV for the near, medium, and far configurations, respectively, significantly extending its light absorption range into the visible region while causing a substantial decrease in reflectivity. Therefore, V and Co co-doped $SrTiO_3$ can not only split water for hydrogen production under visible light but also significantly enhances its photocatalytic efficiency by reducing the recombination centers for photogenerated carriers.

Author contributions

Chuang Li: writing – review & editing, writing – original draft, methodology, investigation. Xianwen Luo: writing – review & editing, methodology, supervision, investigation, funding acquisition. Jiazheng Qiu: writing – review & editing, supervision, project administration. Jianfeng Wen – supervision, investigation, project administration.

Conflicts of interest

The authors declare that they have no known competing financial interests or personal relationships that could have appeared to influence the work reported in this paper.

Data availability

Data will be made available on request.

Acknowledgements

Project supported by the National Natural Science Foundation of China (Grant No. 11405166), the research foundation of Guilin University of Technology (Grant No. GUTQDJJ 2019177). We are thankful to Pro. Shujun Rong for his great help, and we also sincerely appreciate Pro. Xing Ming for his valuable advice.

References

1 Y. Y. Pai, A. Tylan-Tyler, P. Irvin and J. Levy, Physics of $SrTiO_3$-based heterostructures and nanostructures: a review, *Rep. Prog. Phys.*, 2018, **81**, 036503, DOI: 10.1088/1361-6633/aa892d.

2 J. Hwang, R. R. Rao, L. Giordano, Y. Katayama, Y. Yu and Y. Shao-Horn, Perovskites in catalysis and electrocatalysis, *Science*, 2017, **358**, 751–756, DOI: 10.1126/science.aam7092.

3 R. Wang, M. Mujahid, Y. Duan, Z. K. Wang, J. Xue and Y. Yang, A review of perovskite solar cell stability, *Adv. Funct. Mater.*, 2019, **29**, 1808843, DOI: 10.1002/adfm.201808843.

4 S. Zhang, E. Jiang, J. Wu, Z. Liu, Y. Yan, P. Huo and Y. Yan, Visible-light-driven GO/RH-$SrTiO_3$ photocatalyst for efficient overall water splitting, *Catalysts*, 2023, **13**, 851, DOI: 10.3390/catal13050851.

5 X. Li, U. Simon, M. F. Bekheet and A. Gurlo, Mineral-supported photocatalysts: a review of materials, mechanisms and environmental applications, *Energies*, 2022, **15**, 5607, DOI: 10.3390/en15155607.

6 S. Jouybar, L. Naji, S. A. Mozaffari and S. Sarabadani Tafreshi, In situ electrochemical cobalt doping in perovskite-structured lanthanum nickelate thin film toward energy conversion enhancement of polymer solar cells, *ACS Appl. Mater. Interfaces*, 2024, **16**, 32857–32873, DOI: 10.1021/acsami.4c04669.

7 M. J. Nunes, A. Lopes, M. J. Pacheco and L. Ciríaco, Visible-light-driven AO_7 photocatalytic degradation and toxicity removal at Bi-doped $SrTiO_3$, *Materials*, 2022, **15**, 2465, DOI: 10.1134/S0036024424040319.

8 Y. Zhao, X. Su, D. Qing, J. Peng, X. Wang, J. Wang and X. Zeng, $WO_3/SrTiO_3$ heterojunction composite: a promising photoanode for photochemical cathodic protection, *Russ. J. Phys. Chem. A*, 2024, **98**, 795–804, DOI: 10.1134/S0036024424040319.

9 B. Gul, M. M. A. Al-Hmoud, M. S. Khan and S. M. Aziz, A comparative DFT study of different structures of ZnTe: for optoelectronic and thermoelectric applications, *RSC Adv.*, 2025, **15**(20), 15550–15560, DOI: 10.1039/D5RA01399B.

10 P. M. Rajaitha, S. Hajra, M. Sahu, K. Mistewicz, B. Toroń, R. Abolhassani and H. J. Kim, Unraveling highly efficient nanomaterial photocatalyst for pollutant removal: a comprehensive review and future progress, *Mater. Today Chem.*, 2022, **23**, 100692, DOI: 10.1016/j.mtchem.2021.100692.

11 S. Demir, M. Torkashvand, S. Jouybar, Z. Nikfarjam, F. Zargari, S. S. Tafreshi and A. Tekin, Hydrogen storage in trimetallic borohydrides: a crystal structure prediction and *ab initio* molecular dynamics simulations study, *J. Phys. Chem. C*, 2023, **127**, 19344–19355, DOI: 10.1021/acs.jpcc.3c02943.

12 M. A. Hassaan, M. A. El-Nemr, M. R. Elkatory, S. Ragab, V. C. Niculescu and A. El Nemr, Principles of photocatalysts and their different applications: a review, *Top. Curr. Chem.*, 2023, **381**, 31, DOI: 10.1007/s41061-023-00444-7.

13 C. Xue, S. Hu, Q. Chang, Y. Li, X. Liu and J. Yang, Fluoride doped $SrTiO_3/TiO_2$ nanotube arrays with a double layer walled structure for enhanced photocatalytic properties and bioactivity, *RSC Adv.*, 2017, **7**, 49759–49768, DOI: 10.1039/C7RA07741F.

14 L. Yu, X. Yang, J. He, Y. He and D. Wang, One-step hydrothermal method to prepare nitrogen and lanthanum co-doped TiO_2 nanocrystals with exposed {0 0 1} facets and study on their photocatalytic activities in visible light, *J. Alloys Compd.*, 2015, **637**, 308–314, DOI: 10.1016/j.jallcom.2015.03.035.

15 S. Jouybar, L. Naji, S. A. Mozaffari, S. S. Tafreshi and N. H. de Leeuw, Electrochemically engineered lanthanum nickelate as a promising transparent hole-transport layer for bulk heterojunction polymer solar cells: an experimental and DFT study, *ACS Appl. Energy Mater.*, 2024, **7**, 1647–1665, DOI: 10.1021/acsaem.3c03274.

16 D. S. Jayalakshmi and B. Nivetha, First-principles calculations for comparative band structure study of $SrTiO_3$ perovskite on bulk and layered phases for efficient optoelectronic conversion, *Comput. Theor. Chem.*, 2023, **1220**, 114006, DOI: 10.1016/j.comptc.2022.114006.

17 W. Wang, M. O. Tadé and Z. Shao, Nitrogen-doped simple and complex oxides for photocatalysis: a review, *Prog. Mater. Sci.*, 2018, **92**, 33–63, DOI: 10.1016/j.pmatsci.2017.09.002.

18 P. Willke, J. A. Amani, A. Sinterhauf, S. Thakur, T. Kotzott, T. Druga and M. Wenderoth, Doping of graphene by low-energy ion beam implantation: structural, electronic, and transport properties, *Nano Lett.*, 2015, **15**, 5110–5115, DOI: 10.1021/acs.nanolett.5b01280.

19 L. Sun, H. W. Zhao, H. Y. Zhao, W. Lu, J. W. Guo, Y. Cao and Z. W. Liu, Overview of high intensity ion source development in the past 20 years at IMP, *Rev. Sci. Instrum.*, 2020, **91**, 02A703, DOI: 10.1063/1.5129399.

20 X. Wang, W. Wan, S. Shen, H. Wu, H. Zhong, C. Jiang and F. Ren, Application of ion beam technology in (photo)

electrocatalytic materials for renewable energy, *Appl. Phys. Rev.*, 2020, **7**, 041301, DOI: 10.1063/5.0021322.

21 X. Zhang, Y. Lv, S. Fu, Y. Wu, X. Lu, L. Yang and Z. Dong, Synthesis, microstructure, anti-corrosion property and biological performances of Mn-incorporated Ca-P/TiO_2 composite coating fabricated *via* micro-arc oxidation, *Mater. Sci. Eng., C*, 2020, **117**, 111321, DOI: 10.1016/j.msec.2020.111321.

22 X. Chen, S. Su, X. Wang, X. Chen, S. A. Ahmad, L. Xu and W. Zhang, First-principles investigations of electronic property modulation in the $FeCl_3$/$MoSi_2N_4$ heterojunction by strain, interlayer distance and vertical electric field variation, *RSC Adv.*, 2025, **15**(27), 21311–21325, DOI: 10.1039/D5RA02387D.

23 A. El Mragui, O. Zegaoui, I. Daou and J. C. G. Esteves da Silva, Preparation, characterization, and photocatalytic activity under UV and visible light of Co, Mn, and Ni mono-doped and (P, Mo) and (P, W) co-doped TiO_2 nanoparticles: a comparative study, *Environ. Sci. Pollut. Res.*, 2021, **28**, 25130–25145, DOI: 10.1007/s11356-019-04754-6.

24 Y. Yamaguchi, S. Usuki, K. Yamatoya, N. Suzuki, K. I. Katsumata, C. Terashima and K. Nakata, Efficient photocatalytic degradation of gaseous acetaldehyde over ground Rh-Sb co-doped $SrTiO_3$ under visible light irradiation, *RSC Adv.*, 2018, **8**, 5331–5337, DOI: 10.1039/C7RA11337D.

25 Y. Wang, J. Wang, W. Lian and Y. Liu, Insight into the enhanced photocatalytic activity of Mo and P co-doped $SrTiO_3$ from first-principles prediction, *RSC Adv.*, 2020, **10**, 40117–40126, DOI: 10.1039/D0RA07026B.

26 I. Shahid, I. Ahmad, A. Ali, A. Raza, X. Zhang, D. Tang and S. A. Abdelmohsen, Square octagon haeckelites as efficient photocatalysts with enhanced solar-to-hydrogen conversion and high carrier mobilities, *Phys. Chem. Chem. Phys.*, 2025, **27**, 13415–13423, DOI: 10.1039/D5CP01522G.

27 A. Raza, I. Shahid, M. Munawar, X. Zhang and D. Tang, First-principles prediction of SiS-Al2SO and blueP-Al2SO vdW heterostructures for high-efficiency photocatalytic water splitting with 23.67% solar-to-hydrogen conversion, *Phys. Chem. Chem. Phys.*, 2025, **27**, 19283–19294, DOI: 10.1039/D5CP02559A.

28 S. Han, M. Wang, D. Cao, Y. Shi, W. Pu, J. Ma and J. Wang, Modification of the band gap of Ruddlesden–Popper perovskites $Sr_{n+1}Ti_nO_{3n+1}$ (n=1, 2, 3, and ∞) by Fe ion irradiation, *Ceram. Int.*, 2023, **49**, 7396–7403, DOI: 10.1016/j.ceramint.2022.10.209.

29 A. Yamakata, M. Kawaguchi, R. Murachi, M. Okawa and I. Kamiya, Dynamics of photogenerated charge carriers on Ni-and Ta-doped $SrTiO_3$ photocatalysts studied by time-resolved absorption and emission spectroscopy, *J. Phys. Chem. C*, 2016, **120**, 7997–8004, DOI: 10.1021/acs.jpcc.6b01494.

30 X. Zhou, J. Shi and C. Li, Effect of metal doping on electronic structure and visible light absorption of $SrTiO_3$ and $NaTaO_3$ (Metal= Mn, Fe, and Co), *J. Phys. Chem. C*, 2011, **115**, 8305–8311, DOI: 10.1021/jp200022x.

31 C. Yang, T. Liu, Z. Cheng, H. Gan and J. Chen, Study on Mn-doped $SrTiO_3$ with first principal calculation, *Physica B*, 2012, **407**, 844–848, DOI: 10.1016/j.physb.2011.12.020.

32 G. Kresse and D. Joubert, From ultrasoft pseudopotentials to the projector augmented-wave method, *Phys. Rev. B: Condens. Matter Mater. Phys.*, 1999, **59**, 1758, DOI: 10.1103/PhysRevB.59.1758.

33 G. Kresse and J. Furthmüller, Efficient iterative schemes for *ab initio* total-energy calculations using a plane-wave basis set, *Phys. Rev. B: Condens. Matter Mater. Phys.*, 1996, **54**, 11169, DOI: 10.1103/PhysRevB.54.11169.

34 J. P. Perdew, K. Burke, M. Ernzerhof, B. Perdew and E. reply, *Phys. Rev. Lett.*, 1998, **80**, 891, DOI: 10.1103/PhysRevLett.80.891.

35 E. Skúlason, G. S. Karlberg, J. Rossmeisl, T. Bligaard, J. Greeley, H. Jónsson and J. K. Nørskov, Density functional theory calculations for the hydrogen evolution reaction in an electrochemical double layer on the Pt (111) electrode, *Phys. Chem. Chem. Phys.*, 2007, **9**, 3241–3250, DOI: 10.1039/C6CP02198K.

36 S. Xue, F. Zhang, S. Zhang, X. Wang and T. Shao, Electronic and magnetic properties of Ni-doped zinc-blende ZnO: a first-principles study, *Nanomaterials*, 2018, **8**, 281, DOI: 10.3390/nano805028.

37 X. Xiao, J. Wang, H. Zhu, L. Liu, Z. Liu and J. Tu, Effects of Nb concentration on Nb-doped anatase TiO_2: DFT + U calculations, *Phys. Scr.*, 2022, **97**, 055819, DOI: 10.1088/1402-4896/ac670a.

38 M. Zhu, S. Lv, B. Xiao, M. Gao and Q. Yang, Doping modulation effect on the electronic structure and catalytic activities of strontium titanate from first-principles investigation, *Int. J. Hydrogen Energy*, 2025, **169**, 151156. https://www.x-mol.com/paperRedirect/1962570647475089408.

39 K. Ehatäht and C. Veelken, Stitching Monte Carlo samples, *Eur. Phys. J. C*, 2022, **82**, 484, DOI: 10.1140/epjc/s10052-022-10407-9.

40 G. H. Al-Malkawi, A. M. B. A. Al-Ajlony and K. F. AL-Shboul, Simulation of ranges and sputtering of low energy Helium and Argon ions irradiation on Tungsten surface, *Radiat. Phys. Chem.*, 2024, **214**, 111296, DOI: 10.1016/j.radphyschem.2023.111296.

41 F. Yang, L. Yang and C. Ai, Doping for visible-light photoelectrical applications: a first-principles study, *Nanomaterials*, 2018, **8**, 455, DOI: 10.3390/nano8070455.

42 C. Ouettar, H. Yahi and H. Chibani, Tuning the magnetic and electronic properties of MoI_3 monolayer by 3d transition metal doping: a first-principles study, *J. Magn. Magn. Mater.*, 2022, **551**, 169163, DOI: 10.1016/j.jmmm.2022.169163.

43 H. Deng, Q. Zhu, C. Kong, G. Tang, J. Cao, T. Han, B. Wang, Y. Yang and H. Lin, Tuning the electronic and magnetic properties of monolayer Mo_8S_{12} *via* defects and 3d transition metal substitutional doping, *J. Magn. Magn. Mater.*, 2023, **588**, 171385, DOI: 10.1016/j.jmmm.2023.171385.

44 H. Bentour, M. El Yadari, A. El Kenz and A. Benyoussef, DFT study of electronic and optical properties of (S–Mn) co-doped $SrTiO_3$ for enhanced photocatalytic hydrogen production, *Solid State Commun.*, 2020, **312**, 113893, DOI: 10.1016/j.ssc.2020.113893.

45 M. Ishfaq, M. Yaseen, F. F. Al-Harbi and M. K. Butt, Tailoring the magneto-electronic and optical properties of cobalt doped strontium titanate by first-principles calculations, *Physica B*, 2023, **664**, 415025, DOI: 10.1016/j.physb.2023.415025.

46 Y. Q. Wang, W. Lian and Y. Liu, Electronic structure and optical properties in alkaline-earth metals (A= Mg, Ca, Ba) and Ir co-doped $SrTiO_3$: a DFT+ U investigation, *Optik*, 2021, **228**, 166128, DOI: 10.1016/j.ijleo.2020.166128.

47 M. Rizwan, Z. Khadija, T. Mahmood, S. S. A. Gillani and M. I. Khan, Alteration impact of electronic properties of c-$SrTiO_3$ on optical response due to Ca inclusion: a DFT study, *Physica B*, 2021, **602**, 412553, DOI: 10.1016/j.physb.2020.412553.

48 W. J. Shi and S. J. Xiong, Ab initio study on band-gap narrowing in $SrTiO_3$ with Nb-C-Nb codoping, *Phys. Rev. B: Condens. Matter Mater. Phys.*, 2011, **84**, 205210, DOI: 10.1103/PhysRevB.84.205210.

49 C. Zhang, Y. Jia, Y. Zhong, Y. Yao, J. Ma and J. Sun, DFT study on electronic structure and optical properties of N-doped, S-doped, and N/S co-doped $SrTiO_3$, *Physica B*, 2012, **407**, 4649–4654, DOI: 10.1016/j.physb.2012.08.038.

50 J. Wang, Y. Wang, Y. Wang, X. Zhang, Y. Fan, Y. Liu and Z. Yi, Role of P in improving V-doped $SrTiO_3$ visible light photocatalytic activity for water splitting: a first-principles study, *Int. J. Hydrogen Energy*, 2021, **46**, 20492–20502, DOI: 10.1016/j.ijhydene.2021.03.147.

51 M. Y. Xiong and S. Yang, First-principles prediction of enhanced photocatalytic activity in La–X (X= Sc, V, Cr, Mn, Fe, Co, Ni, or Cu) co-doped $SrTiO_3$, *Mater. Today Commun.*, 2023, **37**, 107371, DOI: 10.1016/j.mtcomm.2023.107371.

52 W. Wei, Y. Dai, M. Guo, L. Yu, H. Jin, S. Han and B. Huang, Codoping synergistic effects in N-doped $SrTiO_3$ for higher energy conversion efficiency, *Phys. Chem. Chem. Phys.*, 2010, **12**, 7612–7619, DOI: 10.1039/B922399A.

53 Y. Yang, W. Zheng, D. Cheng and D. Cao, Designing transition metal and nitrogen-codoped $SrTiO_3$ (001) perovskite surfaces as efficient photocatalysts for water splitting, *Sustainable Energy Fuels*, 2017, **1**, 1968–1980, DOI: 10.1039/C7SE00219J.

54 M. Gajdoš, K. Hummer, G. Kresse, J. Furthmüller and F. Bechstedt, Linear optical properties in the projector-augmented wave methodology, *Phys. Rev. B: Condens. Matter Mater. Phys.*, 2006, **73**, 045112, DOI: 10.1103/PhysRevB.73.045112.

55 M. Rioult, H. Magnan, D. Stanescu and A. Barbier, Single crystalline hematite films for solar water splitting: Ti-doping and thickness effects, *J. Phys. Chem. C*, 2014, **118**, 3007–3014, DOI: 10.1021/jp500290j.